



Magnetic Imprints of Eruptive and Noneruptive Solar Flares as Observed by Solar Dynamics Observatory

N. Vasantharaju^{1,2} , P. Vemareddy¹ , B. Ravindra¹, and V. H. Doddamani³

¹ Indian Institute of Astrophysics, Koramangala, Bengaluru-560 034, India; vrajuap@gmail.com

² Dipartimento di Fisica e Astronomia “Ettore Majorana” - Sezione Astrofisica, Università degli Studi di Catania, Via S. Sofia 78, I-95123 Catania, Italy

³ Department of Physics, Bangalore University, Bengaluru-560 056, India

Received 2021 August 22; revised 2022 January 12; accepted 2022 January 14; published 2022 March 8

Abstract

The abrupt and permanent changes of the photospheric magnetic field in the localized regions of active regions during solar flares, called magnetic imprints (MIs), have been observed for nearly the past three decades. The well-known coronal implosion model is assumed to explain such flare-associated changes but the complete physical understanding is still missing and debatable. In this study, we made a systematic analysis of flare-related changes of the photospheric magnetic field during 21 flares (14 eruptive and seven noneruptive) using the 135 s cadence vector magnetogram data obtained from the Helioseismic and Magnetic Imager. The MI regions for eruptive flares are found to be strongly localized, whereas the majority of noneruptive events (>70%) have scattered imprint regions. To quantify the strength of the MIs, we derived the integrated change of horizontal field and the total change of Lorentz force over an area. These quantities correlate well with the flare strength, irrespective of whether flares are eruptive or not, or have a short or long duration. Further, the free energy (FE), determined from virial theorem estimates, exhibits a statistically significant downward trend that starts around the flare time and is observed in the majority of flares. The change of FE during flares does not depend on eruptivity but has a strong positive correlation (≈ 0.8) with the Lorentz force change, indicating that part of the FE released would penetrate the photosphere. While these results strongly favor the idea of significant feedback from the corona on the photospheric magnetic field, the characteristics of MIs are quite indistinguishable from flares being eruptive or not.

Unified Astronomy Thesaurus concepts: Solar activity (1475); Solar photosphere (1518); Solar flares (1496); Solar coronal mass ejections (310)

1. Introduction

The magnetic field is believed to be the viable source of energy for the released thermal and radiant energy in solar flares and the observed kinetic energy in coronal mass ejections (CMEs; Forbes 2000; Hudson 2007). It is widely accepted that solar eruptions like flares and CMEs are the result of coronal magnetic restructuring, generally involving magnetic reconnection during which the magnetic free energy gets converted into heat, electromagnetic radiation, and kinetic energy (Priest & Forbes 2002). More than three decades of observational studies (e.g., Patterson & Zirin 1981; Wang 1992; Wang et al. 2012b) confirm that the solar photosphere responds to the sudden coronal magnetic restructuring that occurs during most major flares. The flare-associated changes in the photospheric magnetic field can be “transients” (e.g., Maurya et al. 2012) and “permanent” as well. In this article, we are discussing abrupt, permanent, and widely distributed patterns of magnetic field change associated with flares called magnetic imprints (MIs). Here, the magnetic field change is considered “permanent” if its effect lasts for at least a couple of hours after the flare.

As far as the history of studies on MIs is concerned, Wang (1992) provided the first clear illustration of it using ground-based vector magnetograms. They reported the stepwise enhancement of magnetic shear cotemporal with the initiation of an X3 class flare. Later, Kosovichev & Zharkova (2001), with the help of the line-of-sight (LOS) magnetograms obtained from the Michelson

Doppler Imager (MDI; Scherrer et al. 1995) on board the Solar and Heliospheric Observatory (SOHO; Domingo et al. 1995) satellite, observed the abrupt and permanent magnetic flux decrease near the polarity inversion lines during an X-class flare occurring near the disk center. Zharkova et al. (2005) observed LOS magnetic flux increase during an X-class flare that occurred near the limb. Generally, the LOS magnetic flux increases in the active regions (ARs) located near the limb and decreases in ARs near the disk center, indicating the more horizontal magnetic field configuration (Wang et al. 2002). By availing LOS magnetograms obtained from the Global Oscillations Network Group ground-based network, Sudol & Harvey (2005) found the abrupt, significant, and permanent changes in longitudinal magnetic field strength during 15 X-class flares. By analyzing vector magnetograms obtained from the ground-based vector magnetographs, Wang & Liu (2010) studied 11 X-class flares and found an increase of the transverse field at the polarity inversion line (PIL) of each event source AR.

With the launch of the Solar Dynamics Observatory (SDO), the continuous, high spatial and temporal resolution full-disk vector magnetograms are being obtained from the Helioseismic and Magnetic Imager (HMI; Schou et al. 2012) instrument on board the SDO (Pesnell et al. 2012). Using 12 minute vector magnetograms, rapid and irreversible MIs on the photospheric magnetic field (i.e., leading to a more horizontal magnetic field structure) were observed during several major eruptions (Petrie 2012, 2016; Lu et al. 2019). Wang et al. (2012b) observed MIs on the photospheric magnetic field during 18 different Geostationary Orbiting Earth Satellite or GOES-class flares (including C-class events) and found that the vertical Lorentz force changes during flares were generally directed

downward near PILs and the absolute value of these forces are well correlated with the flare strength. Sun et al. (2017) introduced the high-cadence (90 s and 135 s) vector magnetograms from the HMI to characterize the rapid evolution of the horizontal magnetic field. Many more studies on MIs are summarized in the review article by Toriumi & Wang (2019).

Nevertheless, the physical understanding of flare-associated field changes in the photosphere is yet unclear. Hudson (2000) proposed magnetic implosion conjecture to explain such flare-associated changes in the photosphere. The conjecture claims that magnetic implosion must occur simultaneously with coronal magnetic restructuring during flares/CMEs to lead to the abrupt contraction of the loop structure, making the photospheric magnetic field become more horizontal (Hudson et al. 2008). Further developing this model, Fisher et al. (2012) claimed that the perturbation of the Lorentz force balance results in upward driving of CME mass to a greater speed, and simultaneously the same amount of impulse must act downwards on the photosphere due to momentum conservation. This downward impulse, also known as the “magnetic jerk,” is believed to drive the helioseismic waves into the solar interior (sunquakes; e.g., Kosovichev & Zharkova 1998). Another possible mechanism responsible for the generation of a sunquake is the strong hydrodynamic shocks traveling downward to photospheric levels and solar interior at supersonic speed due to the injection of energetic particle beams into the chromosphere in the flaring atmosphere (Fisher et al. 1985; Zharkova & Zharkov 2015).

Further, the observations of contractions of coronal loop structures during major flares in coronal EUV images (Gosain 2012; Liu et al. 2012; Sun et al. 2012; Simões et al. 2013; Wang et al. 2018) provides clear evidence of coronal implosion as predicted by Hudson (2000). Though we have such a vast accumulation of observational evidence favoring the coronal implosion model, the origin of MIs is still not clear, leading to questions such as: How does the surface magnetic field become more horizontal? Also, recent observational studies (Kleint 2017; Sun et al. 2017) raised many questions on the validity of the coronal implosion model, such as: Would the photospheric magnetic field not respond in a similar manner to that of the contracting coronal field during flares? If ubiquitous observations of MIs all over the AR leads to the neutralization of oppositely directed vertical Lorentz forces, is the resultant upward impulse insufficient to drive the CME outwards?

In the present study, we analyzed 21 flare events in a systematic way by availing the 135 s cadence vector magnetograms and compared them quantitatively to check the validity of the predictions made by Hudson et al. (2008) and Fisher et al. (2012). Meanwhile, we also attempted to address a few questions pertaining to MIs in order to understand the backreaction during flares effectively. Thus, the motivation of this study is threefold: 1. Check the validity of the conjecture (Hudson et al. 2008; Fisher et al. 2012) for a large number of different GOES-class flare events. 2. Assess whether the eruptive flares yield larger magnetic field changes (strength of MIs) on the photosphere compared to noneruptive counterparts. 3. Assess whether the amount of decrease in magnetic free energy during flares has any correspondence with the backreaction on the solar surface. Details of the observational data and methodology are given in Section 2. The analysis and results are described in Section 3. Summary and discussions are given in Section 4.

2. Observational Data, Processing, and Methods

To study the rapid magnetic evolution during solar eruptions, we have used the 135 s vector magnetogram data (hmi.B_135s series) obtained from the HMI on board the SDO. This dataset has the same format and pixel size (0''5) as that of the routine 720 s version of the dataset and is processed with identical pipeline procedures with a few exceptions, which were discussed in Sun et al. (2017). Sun et al. did a detailed comparison indicating that the high-cadence data agrees with the routine version in strong field regions ($B > 300$ G). However, due to higher noise, a caveat should be considered while analyzing the transverse magnetic field in weaker field regions. These high-cadence data series are in native Helioprojective-Cartesian coordinates (field strength, inclination, and azimuth) and these field vectors have to be reprojected into heliocentric spherical coordinates (r , θ , ϕ). For this, we have adapted the HMI pipeline procedures along with several modules under the SolarSoft HMI branch to resolve the azimuth ambiguity (hmi_disambig.pro) and remap the full-disk data into Cylindrical Equal Area (CEA) coordinates (bvec2cea.pro). Finally, the obtained field components (B_p , B_θ , B_ϕ) in heliocentric spherical coordinates were approximated to heliographic components (B_x , $-B_y$, B_z) (Sun 2013).

As the high-cadence HMI data has been processed for selected periods of flaring activity between 2010 August and 2015 November, we have chosen a sample of 21 flare events from 17 ARs, in which 14 are CME associated events (eruptive) and seven are not CME associated ones (noneruptive/confined). We included a few C-class flare events in our sample because many-times weaker flares do not show a decrease in free energy, owing to the uncertainties in vector magnetic field measurements (Vasantharaju et al. 2019). Hence, we accumulated more strong flare events in our sample and all these events are located within 40° from the central meridian of the solar disk to minimize the projection effects. The source ARs of sample flare events, along with magnetic imprint properties and associated CME details, are tabulated in Table 1.

Atmospheric Imaging Assembly (AIA; Lemen et al. 2012), another instrument on board the SDO provides the full-disk ultraviolet (UV; 1600 Å and 1700 Å) images at the cadence of 24 s with a pixel size of 0''6. We have used the AIA 1600 Å images to trace the morphology of flare ribbons that in turn helps in identifying the Region of Interest (ROI) on the vector magnetograms. The methodology we followed in the identification of ROI, computation of Lorentz force, and magnetic free energy will be discussed in the following subsections.

2.1. Lorentz Force

As exemplary cases, we considered four events (two eruptive and two noneruptive) to demonstrate the procedure for the computation of Lorentz force change during flares, and to distinguish the morphological features of MIs between eruptive and noneruptive events. The X5.4 and X1.1 flares are associated with CME eruptions (Figures 1(a)–(d)), whereas the X3.1 and C2.3 flares are not associated with CMEs (Figures 1(e)–(h)).

The procedure to identify the ROI enclosing the flare-related changes in the vector magnetograms is similar to that of Wang et al. (2012b). The rapid and irreversible increase of the horizontal magnetic field, $B_h = \sqrt{B_x^2 + B_y^2}$, in the flaring region can be located approximately with the help of corresponding AIA 1600 Å/1700 Å images. But to specify the exact region of MIs, we constructed the difference image of

Table 1
List of 21 Flare Events from 17 ARs and their Associated Magnetic Properties

S.No	NOAA AR	Date	Loc	GOES class	T_{ini} (UT)	T_{end} (UT)	Int. δB_h ($10^{20}Mx$)	Tot. δF_z ($10^{22}dyne$)	ΔFE ($10^{31}ergs$)	T_{cme} (UT)	V_{cme} ($km\ s^{-1}$)	M_{cme} ($10^{15}g$)
1	11158	20110215	S21W14	X2.2	01:44	02:06	6.1 ± 0.8	4.7 ± 1.1	5.7 ± 4.5	02:24	669	4.3
2	11283	20110906	N14W04	X2.1	22:12	22:34	6.7 ± 0.7	4.9 ± 1.2	5.1 ± 4.3	23:05	575	15.0
3	11283	20110907	N14W18	X1.8	22:32	22:44	6.6 ± 1.0	3.1 ± 0.9	4.0 ± 3.6	23:05	792	1.1
4	11429 ^b	20120309	N15W03	M6.3	03:22	04:18	4.0 ± 1.0	2.2 ± 1.0	...	04:26	950	5.6
5	11890	20131110	S11W15	X1.1	05:08	05:24	5.0 ± 1.0	3.1 ± 0.9	2.0 ± 2.3	05:36	682	2.3
6	12017	20140329	N10W20	X1.0	17:35	18:01	4.9 ± 1.2	1.9 ± 0.9	5.0 ± 4.1	18:12	528	5.0
7	12158	20140910	N15E14	X1.6	17:21	18:20	11.9 ± 0.8	6.1 ± 1.7	5.8 ± 4.2	18:00	1267	21.0
8	12242	20141220	S18W29	X1.8	00:11	00:55	17.3 ± 1.0	9.7 ± 0.7	20.2 ± 8.9	01:25	830	22.0
9	11719	20130411	N09E12	M6.5	06:55	07:29	6.1 ± 1.2	0.9 ± 0.6	3.5 ± 2.9	07:24	861	22.0
10	12371	20150622	N12W08	M6.5	17:39	18:51	18.4 ± 1.2	9.8 ± 1.6	17.2 ± 10.1	18:36	1209	4.4
11	12443	20151104	N08W02	M3.7	13:31	14:13	6.4 ± 2.0	1.0 ± 0.8	6.5 ± 5.3	14:48	578	6.6
12	11429	20120307	N17E29	X5.4	00:02	00:40	20.6 ± 1.4	12.4 ± 2.6	39.9 ± 17.5	00:24	2684	14.0
13	11890	20131108	S14E15	X1.1	04:20	04:30	3.5 ± 0.9	2.7 ± 0.8	9.7 ± 5.8	03:24	497	8.8
14	11882	20131028	S08E34	M4.4	15:07	15:21	2.5 ± 1.0	1.4 ± 0.6	2.2 ± 2.6	15:36	812	9.3
15	11166 ^a	20110309	N08W09	X1.5	23:13	23:39	4.5 ± 1.0	2.9 ± 0.6	5.0 ± 4.1
16	12192 ^a	20141024	S16W21	X3.1	21:07	22:13	18.3 ± 3.1	9.9 ± 2.4	12.3 ± 18.8
17	12297 ^a	20150311	S17E22	X2.2	16:11	16:29	5.3 ± 1.2	5.1 ± 0.8	7.8 ± 5.2
18	11261 ^a	20110730	N16E33	M9.3	02:04	02:21	2.6 ± 0.8	2.1 ± 0.7	2.1 ± 1.0
19	11967 ^a	20140202	S11E05	C9.7	11:45	11:55	7.4 ± 1.3	1.4 ± 0.7	1.7 ± 6.8
20	11158 ^a	20110215	S20W08	C4.8	04:27	04:37	0.8 ± 0.7	0.3 ± 0.6	0.6 ± 2.2
21	12353 ^a	20150523	N07W12	C2.3	17:30	17:41	1.1 ± 1.3	0.6 ± 0.7	0.2 ± 0.5

Notes. T_{ini} and T_{end} : the start and end times of the flares, respectively, are obtained from the GOES catalog. Int. δB_h : integrated change of B_h during the flare. Tot. δF_z : total change of Lorentz force during the flare. ΔFE : decrease in magnetic free energy during the flare. T_{cme} : time of CME structure first appeared on LASCO C2 coronagraph. V_{cme} and M_{cme} : linear speed and mass of CMEs are obtained from the LASCO CME catalog, respectively.

^a Noneruptive flare events.

^b Flare event did not exhibit a decrease in free energy.

horizontal magnetic field (δB_h) observed nearest to flare initial and end times. We then overplotted the contour of level 150 G on the δB_h . It is worth noting here that Sun et al. (2017) claims that the error in the transverse magnetic field for the 135 s cadence data is 50 G higher than that of the routine version of 720 s cadence vector magnetograms. Hence the error (σ) in B_h for the 135 s cadence data is 150 G and the propagation of error in the difference maps of the horizontal magnetic field would be $\sigma \delta B_h = \sqrt{\sigma B_{h,i}^2 + \sigma B_{h,f}^2} \approx 200 G$. The left panels of Figure 1 are the B_z maps at the onset of flares and the contours of B_h enhancements at 200 G (yellow), 300 G (orange) and 400 G (red) are overlotted on the respective B_z maps. In the right panels of Figure 1, we displayed the corresponding snapshots of AIA 1600 \AA observed at their flare peak times. By careful manual inspection of contour regions of δB_h and the corresponding AIA images, we then choose the ROI enclosing the contour region with a level greater than 150 G . The blue boxes represent ROI enclosing the flare-related field change. In this way, the non-flare-related enhancement of the horizontal field is well excluded. Note that the blue boxes enclosing the flare kernels in AIA 1600 \AA images are spatially well correlated with B_h enhancements in the left panels of Figure 1. It should be noted that the distinguishing morphological feature of MI regions produced by eruptive events from that of noneruptive ones is that the MI regions of eruptive flares are more strongly localized than MI regions of noneruptive events. Based on the qualitative assessment of MI regions morphology, it is found that more than 70% of noneruptive events in our sample produce scattered regions of MI. The MI region in Figure 1(e) produced by noneruptive flare X3.1 is scattered whereas the MI regions in Figures 1(a) and 1(c) produced by eruptive events of

X5.4 and X1.1 are more localized. A few noneruptive events ($<30\%$) also produce the compact/localized MI regions (Figure 1(g)). The summation of δB_h over the whole ROI gives the value of the integrated change of B_h and the values computed for sample events are tabulated in column seven of Table 1.

Fisher et al. (2012) provided the approximate expression for the total Lorentz force acting on the atmospheric volume enclosing the flaring AR. The equation for the vertical component of total Lorentz force (F_z) is approximated to be the surface integral of the magnetic field over the photospheric surface (the upper and lateral boundaries are considered to be sufficiently far to ignore their magnetic field contributions) and is given by

$$F_z = \frac{1}{8\pi} \int_A (B_z^2 - B_h^2) dA \quad (1)$$

where dA is the pixel area ($1.3 \times 10^{15} \text{cm}^2$). Fisher et al. (2012) asserted that the total Lorentz force acting outward on the exterior from the interior has the same magnitude but opposite sign as the total Lorentz force acting inward on the interior from the exterior. Using Equation (1), the Lorentz force impulse or changes in the Lorentz force vector acting on the volume at and below the photosphere during a flare can be determined. If we have the photospheric vector magnetic field observations at two times, $t = 0$ the start time of the flare and $t = \delta t$ the end time of the flare, then the changes in the downward Lorentz force (δF_z) during the flare is given by Hudson et al. (2008) and Fisher et al. (2012):

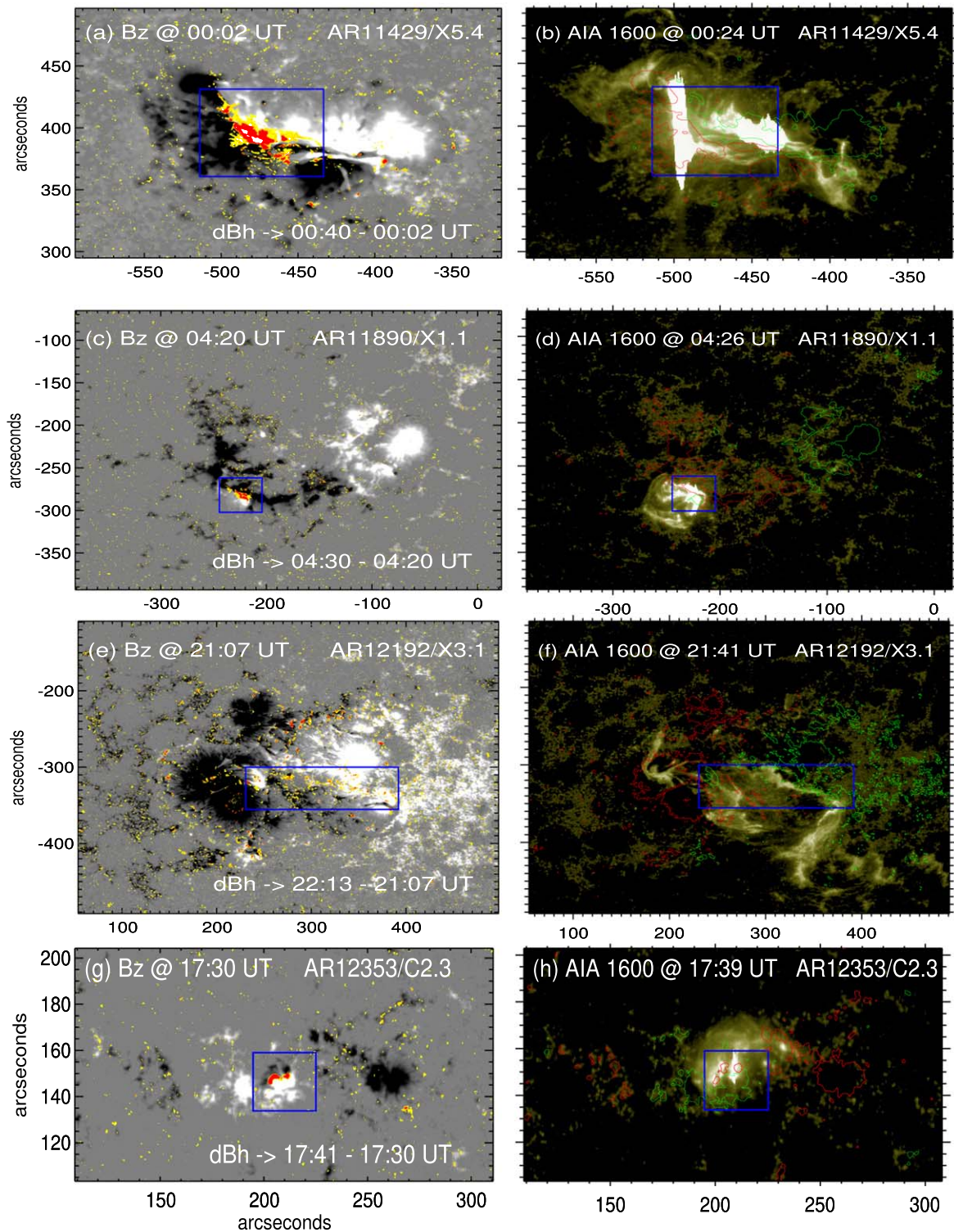


Figure 1. Illustration of four sample events to identify the regions of interest (ROIs) of the magnetic imprints (MIs). The top two events (a–d) are eruptive and the bottom two (e–h) are noneruptive events. (a–b) Eruptive flare event of X5.4 from AR 11429. The B_z map is plotted in panel (a), over which the enhancements of B_h between the flare initial time (00:02UT) and end time (00:40 UT) are plotted. The yellow, orange, and red-filled contours represent the regions with B_h enhancements of 200 G, 300 G, and 400 G, respectively. (b) The AIA 1600 Å image observed at flare peak time (00:24 UT). Overlaid are the B_z contours at ± 600 G. The colored contour region within the blue box in (a) marks the ROI, where the flare kernels in (b) are spatially coherent with the B_h enhancements. The region enclosed by the blue box, which excludes nonflare associated changes, is used for further computations. (c–d) Short-duration eruptive event of X1.1 from AR 11890. (e–f) Noneruptive event of X3.1 from AR 12192, where MIs are scattered. (g–h) Noneruptive event of C2.3 from AR 12353.

$$\delta F_z = \frac{1}{8\pi} \int_A (\delta B_z^2 - \delta B_h^2) dA. \quad (2)$$

It is worth noting that B_z shows no rapid irreversible change in any of our sample events during flares. Therefore, we omitted the term δB_z^2 in Equation (2) while performing computations. Neglecting δB_z^2 in Equation (2) means that the integrand is essentially the same as that in the integral of δB_h , except for the quadratic scaling in the force integral. Consequently, all differences between the integral of δB_h and δF_z will only reflect this difference in scale. The summation of δF_z in the whole ROI gives the value of the integrated Lorentz force change, and the computed values for sample events are tabulated in column 8 of Table 1. The temporal evolution of the horizontal magnetic field and total downward Lorentz force in the ROI are discussed in Section 3.1.

2.2. Magnetic Energy

Given the vector magnetic field observations at the photospheric surface, the total magnetic energy of the AR can be estimated using the virial theorem (Chandrasekhar 1961; Molodensky 1974; Low 1982) and is given by

$$E = \frac{1}{4\pi} \int_S (xB_x + yB_y) B_z dx dy. \quad (3)$$

The assumption involved in the derivation of the above equation is that the photospheric magnetic field is force free, which is not the case with the observations. Also, the finite area surrounding the AR of interest is not fully flux balanced. Though there has been no solid evidence that the virial energy estimate is proportional to magnetic energy in non-force-free fields (NLFFF), we speculate that the virial energy estimate serves as a valid proxy for total magnetic energy in NLFFFs. It is worth noting that the improved virial energy estimate method (Wheatland & Metcalf 2006) provides origin-independent energy estimates. We adopted the Fourier transform method (Gary 1989) to derive the potential magnetic field using the B_z component as input. The minimum energy state is attributed to the current-free or potential field state and any energy excess to it is considered as free energy or nonpotential energy. Subtracting the potential energy (E_p) from the total energy (E) gives the free energy (E_f) available in the AR for energetic events like flares and CMEs. The temporal variations of total, potential, and free energy of our sample events are discussed in Section 3.2.

3. Analysis and Results

3.1. Temporal Evolution of B_h and F_z

As described in Section 2.1, we carefully identified the ROI for each flare event in the sample. We studied the temporal evolution of average B_h and total downward Lorentz force F_z in the ROI by using high-cadence 135 s vector magnetograms for a time window of 4 hr for each event (i.e., ± 2 hr from the flare peak time). The temporal evolution of average B_h and F_z for typical example events of four X-class flares are plotted in the left columns of Figure 2 (top two rows are eruptive and bottom

two rows are noneruptive). A similar evolution for M-class and C-class flares are plotted in Figures 3 (top row is noneruptive flare and remaining three rows are eruptive) and 4 (all three are noneruptive), respectively. For strong field regions, the errors are minimum for HMI 135 s data when compared to weak field regions (Sun et al. 2017). Hence, we assumed a linear variation ($y = -0.03x + 74.44$) of errors (y) from 70 G to 30 G in the $B_x(x)$ and $B_y(x)$ values ranging from 150 to 1500 G, respectively. For the B_x and B_y values having greater than 1500 G, a uniform error of 30 G has been assumed in B_x and B_y . We then propagated these field component errors into the respective equations to finally obtain the errors in the magnetic imprint quantities. We estimated errors on all our computed quantities and plotted them in Figures 2, 3, 4, and 5.

Both B_h and F_z are observed to vary in a stepwise manner during all flare events. In these plots, three vertical dashed lines refer to flare start (black), peak (red), and end times (black), respectively. The horizontal magnetic field rapidly becomes more horizontal during the flare interval (inclination angle rapidly decreases; plot not shown) and this enhancement of B_h is permanent which is in agreement with the past studies (Petrie 2012; Wang et al. 2012b; Sun et al. 2017; Lu et al. 2019). It is worth pointing out here that about 24% (five events) of flare events in our sample are short-time duration events of ≤ 12 m. The average B_h enhancement from their preflare values for short-duration events ranges from 32% to 52%. As an illustration (Figure 2(c)), the flare X1.1 from NOAA 11890 has a duration of 10 minutes and during this short interval, we observed the average B_h enhancement of above 250 G ($>34\%$) from its preflare value. Such rapid changes were able to be recorded more precisely with the help of high-cadence 135 s vector magnetograms than the routine version of 720 s cadence vector magnetograms of HMI. The remaining 76% of flare events in our sample are long-duration events ranging from 13 minutes to more than an hour. These events exhibit the average B_h enhancement from their preflare values in the range of 24%–55%. This shows that the amount of B_h enhancement from its preflare value does not depend much on the duration of flares. However, for longer-duration flares, true flare-associated B_h changes will likely be contaminated by noise from non-flare-related evolution. Unfortunately, we could not quantify the noise estimation from non-flare-related evolution for all the longer-duration flares because HMI 135 s data has been processed for selective time intervals of prominent activity,⁴ leading to unavailability of nonflaring interval data. Nonetheless, the noise estimated for a couple of longer-duration flares in our sample indicates that the contribution of noise effect from non-flare-related evolution is likely smaller than the true flare-related B_h changes. It is worth noting a caveat along with the latter is that the strength of noise from non-flare-related evolution is very subjective.

On the other hand, the total downward Lorentz force shows an abrupt decrease during the flare interval and this change is also irreversible. Here the negative sign assigned to the total Lorentz force represents only the direction, i.e., the force imposed on the photosphere from above as indicated in Equations (1) and (2). The absolute value of the total change of Lorentz force gives a reasonable indicator of the strength of MIs. The computed total δF_z for all the events are tabulated in column 9 of Table 1. As indicated by the strength of MIs tabulated in columns 8 and 9 of

⁴ <http://jsoc.stanford.edu/data/hmi/highcad/>

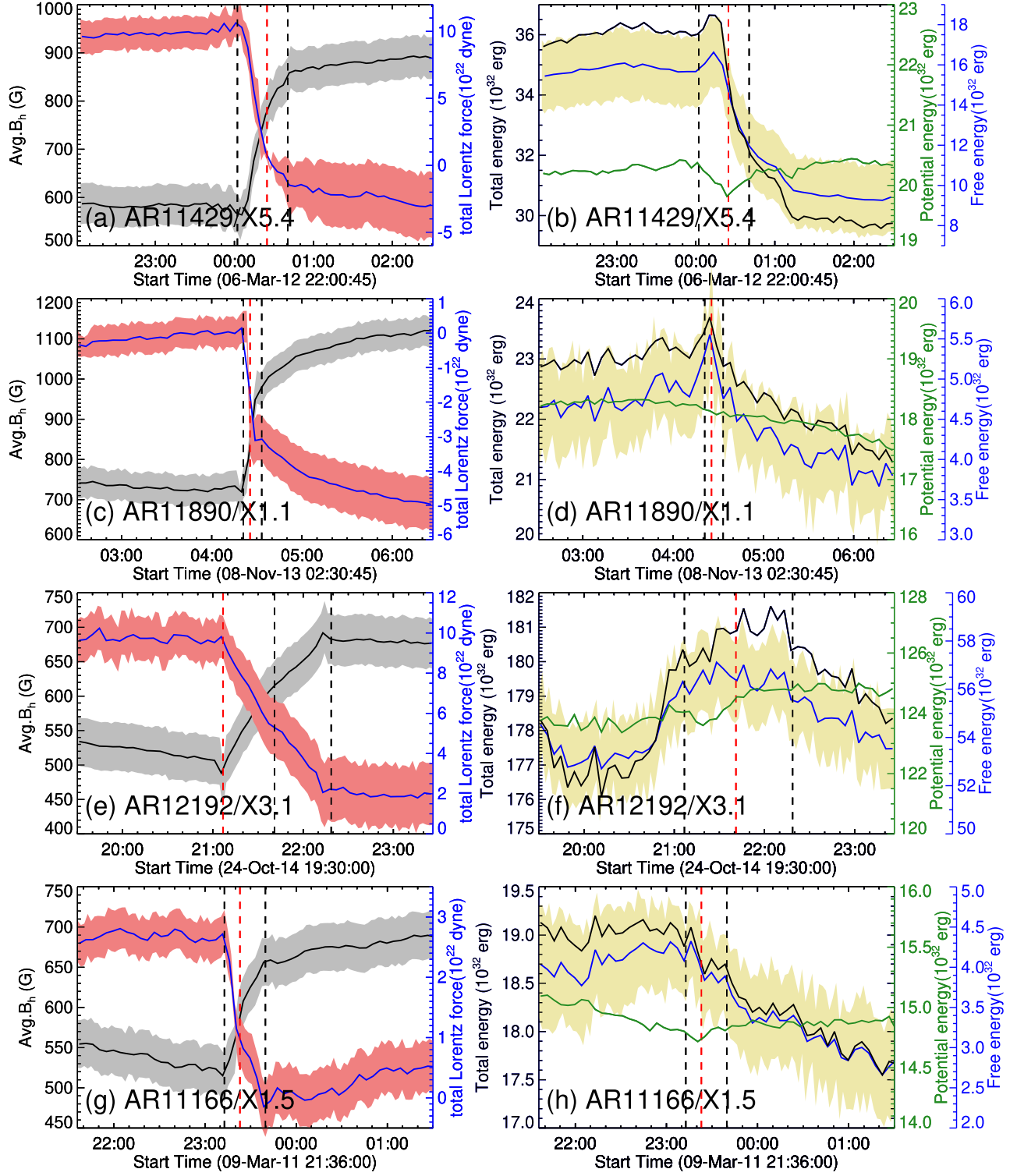


Figure 2. Temporal evolution of magnetic imprints during GOES X-class flares. Top: two events (a–d) are eruptive. Bottom: two (e–h) are noneruptive events. Left column: time evolution of average B_h (black) and the total Lorentz force F_L (blue) over the ROI along with their uncertainties. Right column: the corresponding time evolution of total magnetic energy (black), potential energy (green), and free energy (blue). The pale-yellow shaded region corresponds to the uncertainties in free energy. Note the stepwise changes are cotemporal with flare timings. In all panels, vertical dashed lines refer to flare start (black), peak (red), and end times (black), respectively.

Table 1, it is found that noneruptive flares have a comparable strength of MIs with that of eruptive counterparts. These results suggest that the strength of MIs does not depend on whether the flare is eruptive or not.

3.2. Variation of Magnetic Free Energy

As described in Section 2.2, we computed the total magnetic energy and potential energy using the virial theorem, and the proxy for magnetic free energy is obtained by their difference.

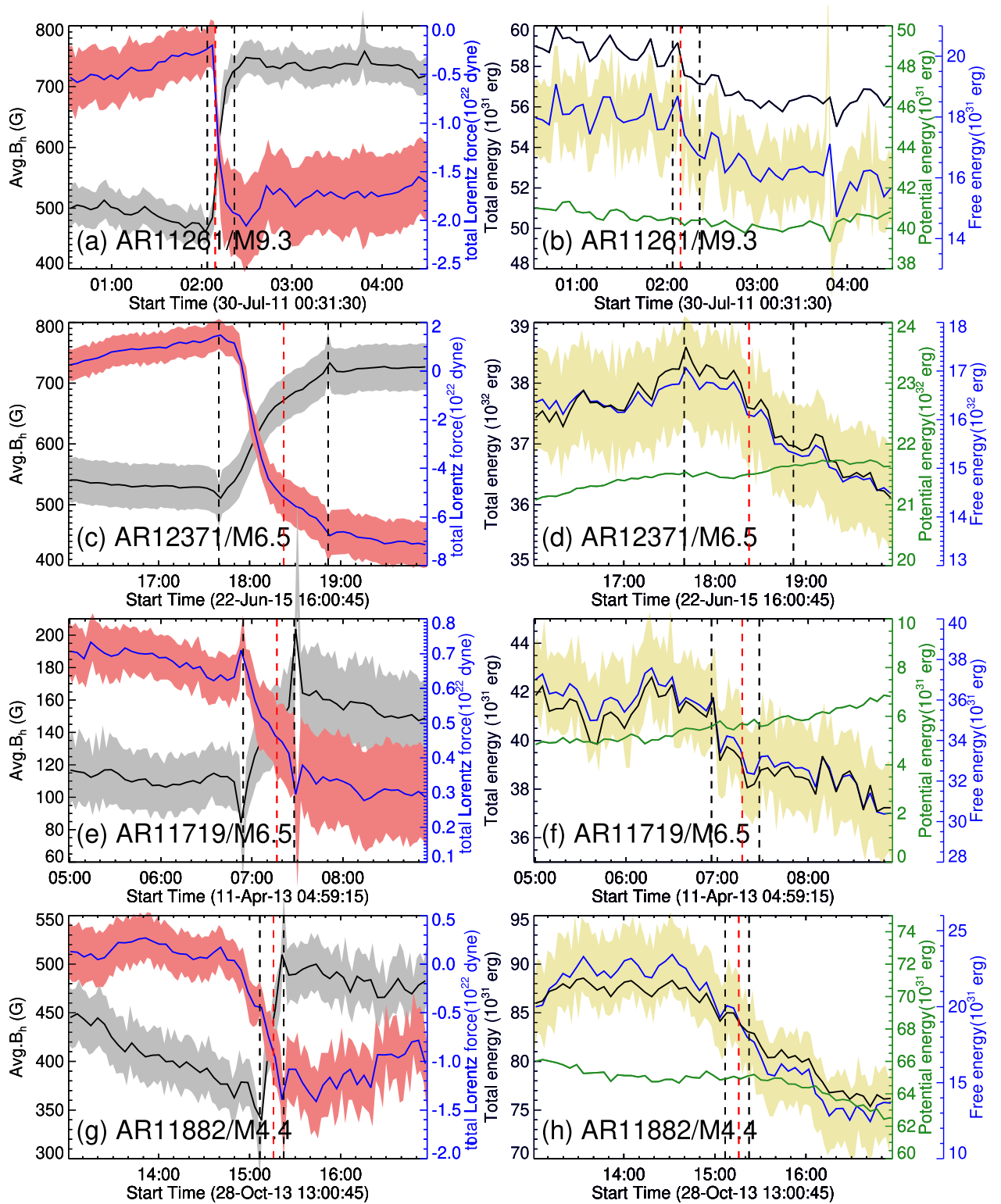


Figure 3. Same as in Figure 2 but for GOES M-class flare events. M9.3 event from AR 11261 is a noneruptive event (a–b) and the remaining events are eruptive (c–h).

For error estimation, we followed the same procedure as described in Section 3.1; the errors in the components of the magnetic field are propagated through the virial theorem to obtain the uncertainties in energy estimates. For greater clarity, only uncertainties in free energy are shown in Figures 2, 3, and 4 as pale-yellow shaded regions. We used the 135 s cadence vector magnetogram data for the time period of 4 hr (± 2 hr from the

flare peak time). For each event, we choose the entire AR such that the flux balance within the region is as good as possible to compute the potential field and to deduce the magnetic energy. Decreases in free energy during several flares in our sample are not statistically significant, but the 14 out of 21 events that exhibit a decrease in free energy exceed the 1σ error level. The temporal evolution of all three magnetic energies for typical

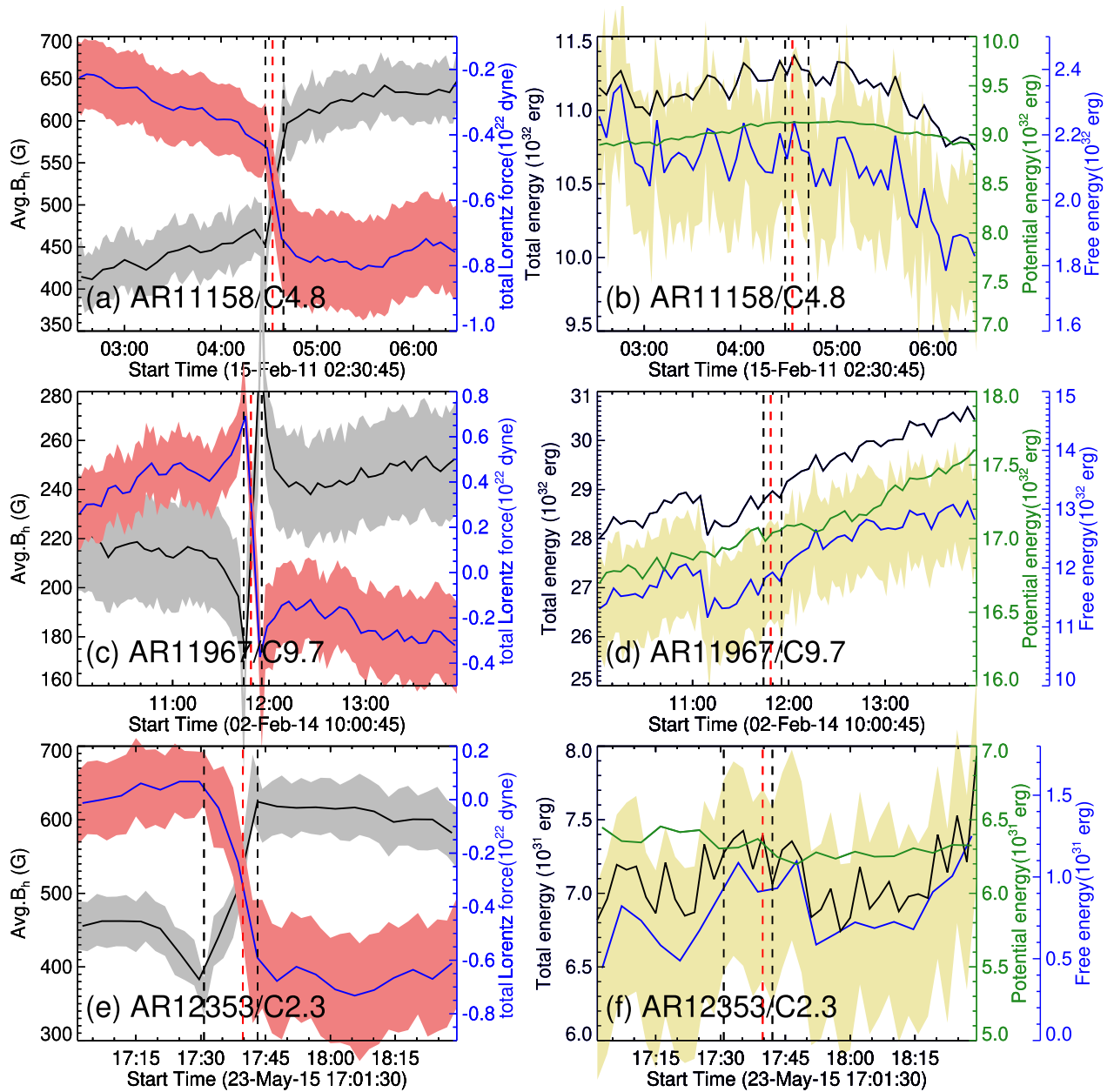


Figure 4. Same as in Figure 2 but for GOES C-class flare events (all three are noneruptive events).

events of X class, M class, and C class are plotted in the right column panels of Figures 2, 3, and 4, respectively. As the potential field only depends upon the B_z component, which is basically unchanged during the given period of evolution, potential energy represented by the green curve in all these panels also remains constant. Consequently, the free energy in blue and total energy in black exhibit the same decreasing trend during and after the flares. These results are in agreement with past studies of individual events (Ravindra & Howard 2010; Vemareddy et al. 2012) and statistical studies (e.g., Vasantharaju et al. 2018). The difference in free energy at the flare start and end times as indicated by the two vertical black dashed lines in all panels of Figures 2, 3, and 4 gives the amount of decrease in free energy (ΔFE). This ΔFE accounts for energy release during flares. The computed values of ΔFE for these 20 events are tabulated in column 9 of Table 1. Estimates of errors for the

change of quantities—integral of δB_h , δF_z , and ΔFE —are also provided in Table 1. The largest amount of free energy released in our sample is about 4×10^{32} ergs during the X5.4 flare event giving out the fastest CME in our sample with a linear speed of 2684 km s^{-1} . The range of amount of free energy released during X-class flare events in our sample is from 2×10^{31} to 4×10^{32} ergs. Similarly, for M-class flares, 2×10^{31} to 1.7×10^{32} ergs, and for C-class flares, 1.8×10^{30} to 1.6×10^{31} ergs. We note that the amount of free energy released during non-eruptive flares is comparable to that of eruptive counterparts. Thus, we opine that the amount of free energy released during a flare has a minimum dependency on whether the flare is eruptive or not. The fluctuations in the free energy seem to be dominated by fluctuations in the total energy.

As an exceptional case in our sample, we did not observe the decrease in free energy during the M6.3 flare from AR

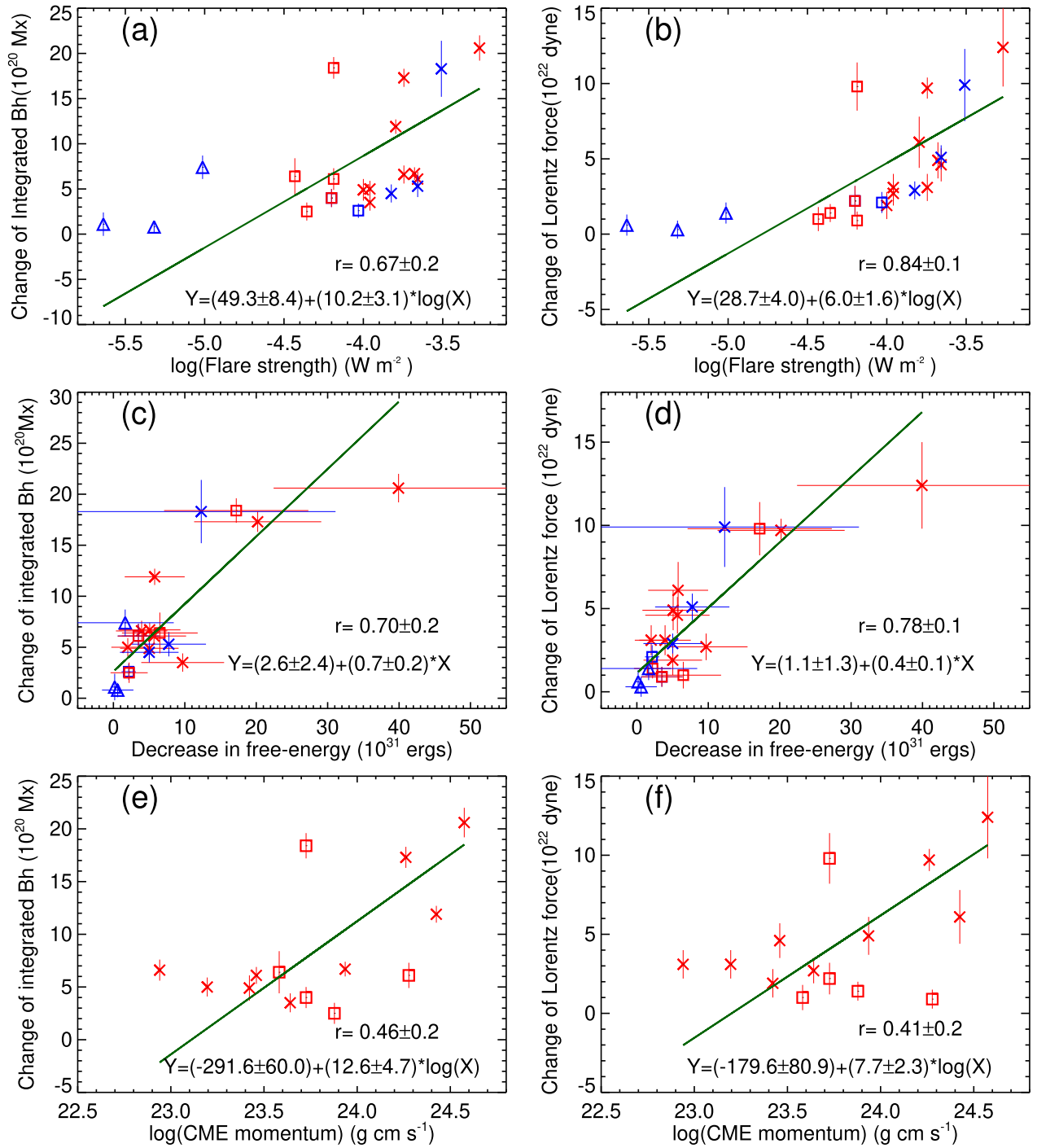


Figure 5. Statistical relation between different physical parameters deduced from magnetic imprint regions. Scatter plots of change of average B_h and δF_z against flare strength (a–b), against free-energy decrease (c–d), against CME linear momentum (e–f). Note the X axes in (a), (b), (e), and (f) are on a logarithmic scale. The Spearman ranking correlation coefficient (r) and the resulting equation for straight-line fit are given in the respective panels. The cross, square, and triangle symbols represent the X-class, M-class, and C-class flares, respectively. The red (blue) colors of these symbols correspond to eruptive (confined) flare cases.

11429. On the contrary, we did find that free energy starts increasing from the flare peak time. AR 11429 is a highly complex $\beta\gamma\delta$ region that produced a sequence of three recurrent M-class flares during 3:00–4:00 UT on 12 March 9 (Simões et al. 2013; Polito et al. 2017). The eruptive M-class white light flare started at 03:22 UT, reached the first maximum in the soft X-ray flux at around 03:27 UT (M1.8 class), and after a small dip in intensity, it rose to M2.1 class at 03:37 UT and further with a small dip it increased up to

about M6.3 class at 3:53 UT. Being a long-duration and recurrent flare event, there is a probability of an increase in magnetic free energy due to the dynamic activity of AR and this is evident in the increase of total flux of AR during the flare (plot not shown). Mostly, this masks the decrease in free energy during the flare. Thus this interesting event is a matter of subjective study and a comprehensive analysis of this event is beyond the scope of our motivations in the present study.

3.3. Statistical Results of Magnetic Imprints

To find the relationship between the MIs and the eruptive properties, we performed the linear regression analysis on the scattered plots shown in Figure 5. The FITEXY routine from the SolarSoft library was employed to carry out the linear regression analysis. This routine is based on a least-square approximation to fit the best straight line, and the standard deviation of both x and y data coordinates are used as error inputs. The slopes and y -intercepts along with their uncertainties obtained from the regression model are shown in the equation of respective panels of Figure 5. The Spearman ranking correlation coefficient (r , referred to as CC) is estimated in all our studies and the standard error in r is estimated by $\text{ERR}_r = \sqrt{(1 - r^2)/(n - 2)}$.

We plotted the log of flare strength against the integrated change of B_h and total change of F_z in Figures 5(a) and 5(b), respectively. The cross, square, and triangle symbols represent the X-class, M-class, and C-class flares, respectively. From these scatter plots, a good correlation is realized (flare strength has a CC of 0.67 with an integrated change of B_h and a CC of 0.84 with a change of F_z) and suggests that stronger flares tend to produce more horizontal field changes, and these changes result in stronger downward impulse on the photosphere. This result is in agreement with Wang & Liu (2010) and Wang et al. (2012b). However, it is worth noting here that two of our eruptive flare events of the same GOES-class strength of M6.5 occurred from NOAA 11719 and NOAA 12371 producing varying strength of MIs on the photospheric magnetic field. The M6.5 from NOAA 12371 produces stronger MIs than the M6.5 from NOAA 11719 (see Table 1). Thus, the strength of the flare may not be the only indicator of the magnitude of the MIs produced. Also, we do not see any evident relationship between the strength of MIs and the eruptive/noneruptive nature of flares. The blue (red) color symbols correspond to noneruptive (eruptive) flares in Figure 5. It should be noted that the strength of MIs produced is less likely dependent on the eruptive or noneruptive nature of flares but more likely depends on the strength of the flares.

Figures 5(c) and (d) display the scatter plots for the amount of the free energy decrease against the integrated δB_h and total δF_z , respectively. We excluded the event M6.3 from AR 11429 in the scatter plot as it exhibits the increase in free energy during a flare. The ΔFE has a CC of 0.70 with integrated δB_h and 0.78 with total δF_z referring to a good correlation. This indicates that the amount of energy released in the corona during flares is strongly related to the photospheric field changes and in turn the downward Lorentz force impulse on the photosphere. It means that the more free energy released during flares, the stronger the MIs produced. From the scatter plots, it is also evident that stronger flares release a larger amount of energy irrespective of being eruptive or not and in turn produce stronger MIs.

To find the relationship between CME eruption and photospheric field changes during flares, we used the properties of 14 eruptive events in our sample. Based on the conservation of linear vertical momentum, Fisher et al. (2012) suggest that the upward impulse from the Lorentz force change drives the magnetic eruption, and the impulse can be related to CME linear momentum. CME linear momentum is computed using the CME mass (M) and linear speed (v) obtained from the Large Angle and Spectrometric Coronagraph (LASCO) CME catalog.⁵ The generated scatter plots are shown in panels (e)

and (f) of Figure 5. The CME linear momentum has the CC of 0.46 with the integrated δB_h and 0.41 with δF_z . The CME linear speed has the CC of 0.52 with the integrated δB_h and 0.45 with δF_z (plot not shown). It indicates that a large change of Lorentz force leads to a stronger upward impulse that drives stronger CMEs. This result is in agreement with the recent study of Lu et al. (2019). We conclude that this weak correlation is mostly due to the poor CME mass estimates in the CDAW CME catalog (Vourlidas et al. 2002, pp. 91–94). The involved assumptions in the CME momentum estimate are that the entire mass of the CME structure moves with uniform speed, and work done against gravity is neglected, which may differ from the ideal case of momentum change proportional to the product of average Lorentz force and the time period over which it acts.

4. Summary and Discussion

We studied the flare-associated changes in the photospheric magnetic field during the 21 flare events of varying GOES-class strengths from C class to X class (14 eruptive and seven noneruptive events) from 17 ARs using recently released and selectively processed 135 s cadence HMI full-disk vector magnetograms. The summary of the main data analysis results obtained are as follows:

1. We observed the rapid and permanent changes on the surface magnetic field in and around the flaring PIL regions of AR. The observed stepwise enhancement in the horizontal field component leads to stepwise changes of Lorentz force over the manually selected ROIs. The average B_h enhancement from their preflare values is in the range of 24%–55%. The MI regions produced by the eruptive flare events in our sample are strongly localized, whereas MI regions produced by the majority of noneruptive events (>70%) are observed to be scattered.
2. The changes of horizontal field integrated over ROI and the magnitude of the downward impulse (produced from the change of Lorentz force), both termed as strength of MIs, are well correlated with the strength of flares having a CC of 0.67 and 0.84, respectively. It is found that irrespective of flares being eruptive or not, with a short (≤ 12 minutes) or long duration (> 13 minutes), stronger flares tend to produce stronger MIs on the surface magnetic field.
3. The magnetic free energy released during the flares under study, estimated using the virial theorem over the whole ARs, shows a strong correlation (CC = 0.78) with the downward impulse imposed on the photosphere. It is noted that stronger flares irrespective of whether they are eruptive or not release a larger amount of free energy that in turn produces stronger MIs.
4. The magnetic free energy exhibits a statistically significant downward trend that starts around the flare time and is observed in the majority (14 of 21) of our strong flares.
5. Due to the lack of reliable CME mass estimates, we were constrained to find the relationship between CME linear speed and the strength of MIs produced. The positive correlation (CC ≈ 0.5) between them indicates that a stronger upward impulse, produced by a larger change of Lorentz force, drives the CME faster.

In the same line of argument as that of result 3, the recent statistical study of Vasantharaju et al. (2018) showed that the

⁵ https://cdaw.gsfc.nasa.gov/CME_list/

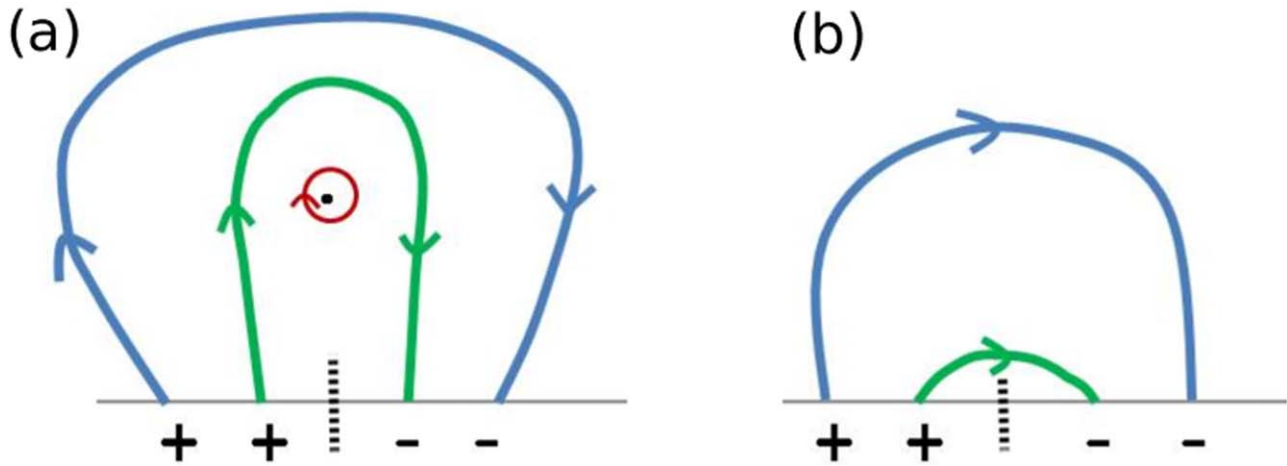


Figure 6. Schematic representation of core magnetic field becoming more horizontal after the implosion in a flaring AR. (a) During pre-eruption, the core field enclosing the flux rope (red circle) indicated by the green curve is mostly vertical in nature while the peripheral magnetic field lines represented by the blue curve are tilted away from the core or roughly horizontal in nature. In contrast, in the post-eruption scenario as depicted in (b), implosion makes the core field become more horizontal and the peripheral field more vertical.

released magnetic free energy is well correlated to the intensity of flares (including 38 eruptive and 39 noneruptive flares). These studies imply that it is hard to use criteria to distinguish between eruptive and noneruptive flare events in terms of released magnetic free energy.

Further, Hudson et al. (2008) and Fisher et al. (2012) suggested that preflare magnetic field configuration is under the equilibrium of balanced forces. This equilibrium of force balance gets disrupted by the rapid release of coronal free energy during flares. The unbalanced Lorentz force change drives the eruption impulse in the upward direction and, due to conservation of momentum, there should be an equal and opposite impulse acting on the plasma of the solar interior to produce the magnetic jerk or “McClymont jerk.” Also, Emslie & Sturrock (1982), using their analytical model, showed that considerable wave energy can penetrate the photosphere and disturb the magnetic field there. Anwar et al. (1993) made a rough estimation of how much transmitted energy goes into seismic waves. In this study, we found a strong association of flare energy released with the magnitude of Lorentz force change. This result favors the idea of coupling flare energy into a seismic wave identified as a magnetic jerk in the solar interior, which is produced by the downward impulse due to the change of Lorentz force during the flares. These observational results and their relationship with the eruption properties reveal that the photospheric magnetic fields respond to the backreaction of coronal field restructuring due to flare energy release, which strongly agrees with the coronal implosion notion of Hudson (2000) and Hudson et al. (2008).

According to the coronal implosion model (Hudson 2000), the core of the AR, as indicated by the green curve in Figure 6, around the flaring PIL, contains a nonpotential structure that exerts outward magnetic pressure on surrounding regions of the AR. This pressure can cause the surrounding fields (blue curve in Figure 6(a)) to tilt away from the core. During a flare (eruptive or not), the core field loses energy and in turn magnetic pressure decreases, and eventually the field becomes more compact as shown in the green curve of Figure 6(b). In contrast, the fields that were tilted away from the core before the flare could become less tilted away from the core or more

vertical as depicted by the blue curve in Figure 6(b). However, many recent observational studies (Kleint 2017; Sun et al. 2017) questioned the validity of the implosion. The model claims that contracting coronal structure leads to the increase of horizontal magnetic fields in the photosphere. But Kleint (2017) showed that chromospheric fields do not evolve in coherence with the photospheric field. This indicates coronal field evolution need not be similar to photospheric field evolution and expresses doubt on the origin of MIs suggested by the model.

Also, Fisher et al.’s (2012) model, which explains the relationship between magnetic eruption and the photospheric magnetic field and changes over the course of a solar flare, contradicts our observations. Following is the illustration of such a contradictory observation with one of our sample events. During the X1.5 flare from AR NOAA 11166, we observed the increase and decrease of B_h values of more than 150 G (up to 350 G) during the flare over almost an entire AR, represented by blue and red contour regions, respectively, as shown in Figure 7(a). The increment and decrement regions of B_h are usually observed to occur adjacent to each other. To study the flare-associated changes in the AR, the green box in panels (a) and (b) of Figure 7 are chosen in such a way that flare kernels should be spatially coherent with the increments and decrements of B_h . The B_h increment regions are prominently observed near the flaring PIL and the B_h decrement regions mostly occur around the polarity regions. The temporal evolution of B_h and the derived Lorentz force in these regions are shown in panels (c) and (d) of Figure 7. These plots imply that the cotemporal increase and decrease of B_h results in the Lorentz forces acting in opposite directions simultaneously. The total positive change of Lorentz force (3.24×10^{22} dyne) due to the increase of B_h gets canceled by the negative change of Lorentz force (-3.09×10^{22} dyne) due to decrease of B_h within the volume lying above the surface region enclosed by the green box in Figure 7, whereas the B_z variations during the flare as shown in panels (e) and (f) of Figure 7 did not exhibit any flare-associated permanent changes. Thus, the increase and decrease of B_h lead to the cancellation of oppositely directed Lorentz forces, and the net upward impulse will be insufficient

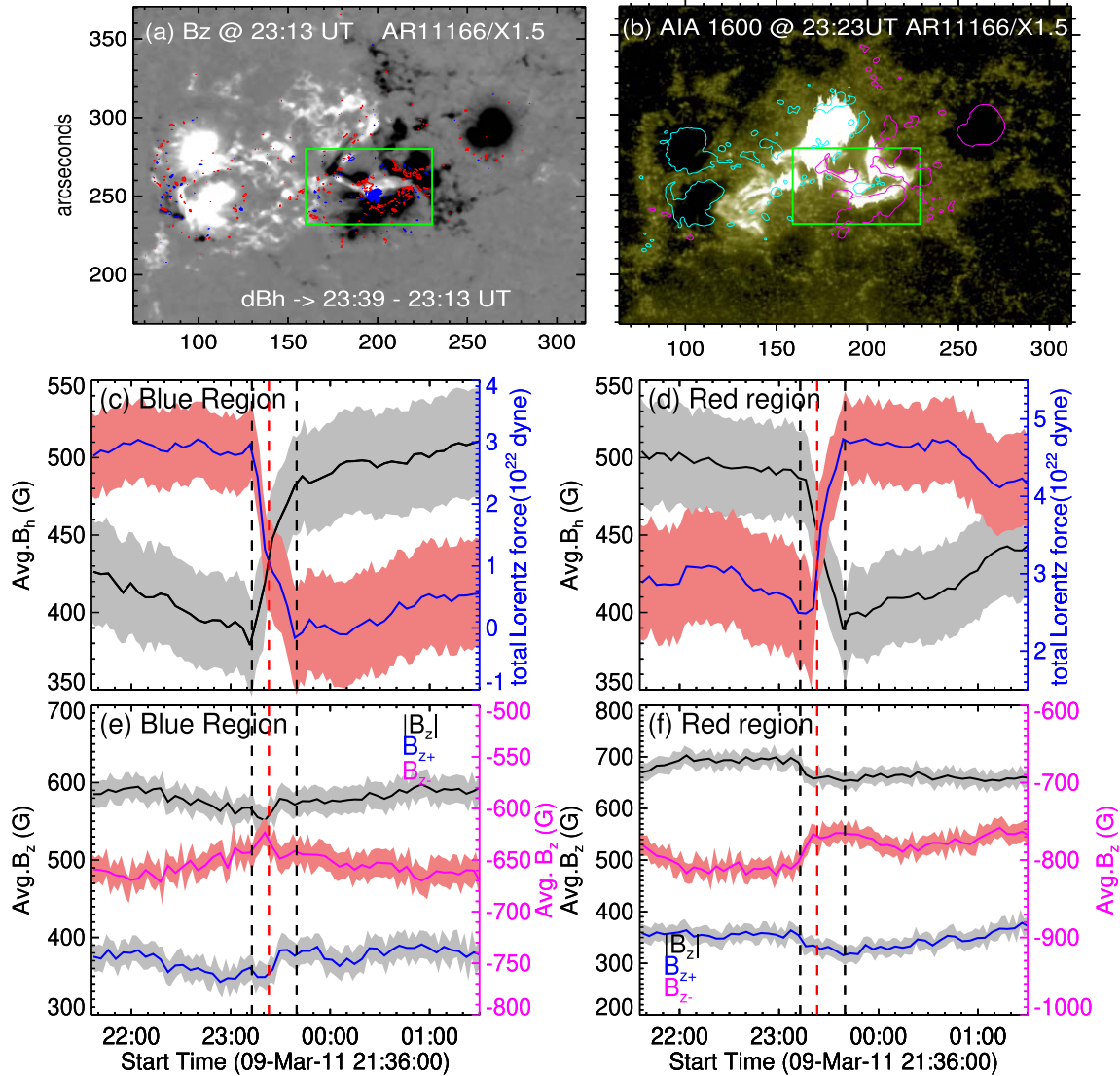


Figure 7. An example of a noneruptive flare event (X1.5 from AR 11166) illustrating the cancellation of Lorentz forces. (a) B_z map overlaid with the blue and red contours of B_h increments (200 G and 300 G) and decrements (-200 G and -300 G) during the flare start time (23:13 UT) and end time (23:39 UT), respectively. (b) AIA 1600 Å image observed at flare peak time (23:23 UT); overlaid are the B_z contours at ± 600 G. The green box in these two panels is the ROI where the flare kernels in panel (b) are spatially correlated with the increments and decrements of B_h in panel (a). (c) Temporal evolution of average B_h and derived Lorentz force over the B_h incremented (blue) regions within the green box of (a). (d) Same as (c) but over the B_h decremented (red) regions enclosed by the green box of (a). (e)–(f) Temporal evolution of absolute B_z and net flux in the blue and red regions within the green box of (a), respectively. Note the Lorentz forces are acting in opposite directions within the green box and variations of B_z show no predominant irreversible changes during the flare.

to drive the CME momentum, making a contradiction to the model proposed by Fisher et al. (2012).

Likewise, many observations related to MIs are not yet understood completely. We observed the increase (stepwise) of nonpotential parameters like total current, twist parameter (α), magnetic shear/weighted shear angle, and the horizontal component of the magnetic field during flares. As the vertical magnetic field remains constant throughout the flare, we expect the magnetic free energy to increase (according to Equation (3)) but actually it decreases during flares. Though there were attempts at explaining how the magnetic field becomes more horizontal during flares using the tether-cutting reconnection model (e.g., Wang et al. 2012a) or enhancement of nonpotentiality due to the emergence of sheared fields (Jing et al. 2008), by and large, the origin of MIs is still an open

question. These contradictions indicate the need for a general model to help us better understand the origin of MIs.

The authors thank the reviewer for insightful comments and suggestions that greatly improved the quality of the manuscript. The authors also thank Dr. Manolis K. Georgoulis, the AAS Journals Scientific Editor, for providing useful comments and suggestions. The version of the cartoon concept, which is employed as Figure 6 in the manuscript, was initially suggested by the reviewer. The SDO is a mission of NASA’s Living With a Star program. We thank the HMI science team for the open data policy of high-cadence vector magnetograms. The CME catalog is generated and maintained at the CDAW Data Center by NASA and The Catholic University of America in cooperation with the Naval

Research Laboratory. SOHO is a project of international cooperation between ESA and NASA. V.N. acknowledges support from the European Union's Horizon 2020 research and innovation programme under grant agreement No. 824135 (SOLARNET project) and No. 739500 (PRE-EST project). This research has been carried out in the framework of the CAESAR (Comprehensive spACE wEather Studies for the ASPIS prototype Realization) project. V.N. acknowledges financial contribution from the Agreement ASI-INAF n.2020-35-HH.0. This work was also supported by the Italian MIUR-PRIN grant 2017APKP7T, by the Università degli Studi di Catania (Piano per la Ricerca Università di Catania 2020-2022, Linea di intervento 2).

ORCID iDs

N. Vasantharaju  <https://orcid.org/0000-0003-2336-5208>
 P. Vemareddy  <https://orcid.org/0000-0003-4433-8823>

References

- Anwar, B., Acton, L. W., Hudson, H. S., et al. 1993, *SoPh*, **147**, 287
 Chandrasekhar, S. 1961, *Hydrodynamic and hydromagnetic stability* (Oxford: Clarendon)
 Domingo, V., Fleck, B., & Poland, A. I. 1995, *SoPh*, **162**, 1
 Emslie, A. G., & Sturrock, P. A. 1982, *SoPh*, **80**, 99
 Fisher, G. H., Bercik, D. J., Welsch, B. T., & Hudson, H. S. 2012, *SoPh*, **277**, 59
 Fisher, G. H., Canfield, R. C., & McClymont, A. N. 1985, *ApJ*, **289**, 414
 Forbes, T. G. 2000, *JGR*, **105**, 23153
 Gary, G. A. 1989, *ApJS*, **69**, 323
 Gosain, S. 2012, *ApJ*, **749**, 85
 Hudson, H. S. 2000, *ApJL*, **531**, L75
 Hudson, H. S. 2007, in ASP Conf. Ser. 368, *The Physics of Chromospheric Plasmas*, ed. P. Heinzel, I. Dorotovič, & R. J. Rutten (San Francisco, CA: ASP), 365
 Hudson, H. S., Fisher, G. H., & Welsch, B. T. 2008, in ASP Conf. Ser. 383, *Flare Energy and Magnetic Field Variation*, ed. R. Howe (San Francisco, CA: ASP), 221
 Jing, J., Wiegmann, T., Suematsu, Y., Kubo, M., & Wang, H. 2008, *ApJL*, **676**, L81
 Kleint, L. 2017, *ApJ*, **834**, 26
 Kosovichev, A. G., & Zharkova, V. V. 1998, *Natur*, **393**, 317
 Kosovichev, A. G., & Zharkova, V. V. 2001, *ApJL*, **550**, L105
 Lemen, J. R., Title, A. M., Akin, D. J., Boerner, P. F., et al. 2012, *SoPh*, **275**, 17
 Liu, C., Deng, N., Liu, R., Lee, J., et al. 2012, *ApJL*, **745**, L4
 Low, B. C. 1982, *SoPh*, **77**, 43
 Lu, Z., Cao, W., Jin, G., Zhang, Y., Ding, M., & Guo, Y. 2019, *ApJ*, **876**, 133
 Maurya, R. A., Vemareddy, P., & Ambastha, A. 2012, *ApJ*, **747**, 134
 Molodensky, M. M. 1974, *SoPh*, **39**, 393
 Patterson, A., & Zirin, H. 1981, *ApJL*, **243**, L99
 Pesnell, W. D., Thompson, B. J., & Chamberlin, P. C. 2012, *SoPh*, **275**, 3
 Petrie, G. J. D. 2012, *ApJ*, **759**, 50
 Petrie, G. J. D. 2016, *SoPh*, **291**, 791
 Polito, V., Del Zanna, G., Valori, G., et al. 2017, *A&A*, **601**, A39
 Priest, E. R., & Forbes, T. G. 2002, *A&ARv*, **10**, 313
 Ravindra, B., & Howard, T. A. 2010, *BASI*, **38**, 147
 Scherrer, P. H., Bogart, R. S., Bush, R. I., Hoeksema, J. T., et al. 1995, *SoPh*, **162**, 129
 Schou, J., Scherrer, P. H., Bush, R. I., Wachter, R., Couvidat, S., et al. 2012, *SoPh*, **275**, 229
 Simões, P. J. A., Fletcher, L., Hudson, H. S., & Russell, A. J. B. 2013, *ApJ*, **777**, 152
 Sudol, J. J., & Harvey, J. W. 2005, *ApJ*, **635**, 647
 Sun, X. 2013, arXiv:1309.2392
 Sun, X., Hoeksema, J. T., Liu, Y., Kazachenko, M., & Chen, R. 2017, *ApJ*, **839**, 67
 Sun, X., Hoeksema, J. T., Liu, Y., Wiegmann, T., et al. 2012, *ApJ*, **748**, 77
 Toriumi, S., & Wang, H. 2019, *LRSP*, **16**, 3
 Vasantharaju, N., Vemareddy, P., Ravindra, B., & Doddamani, V. H. 2018, *ApJ*, **860**, 58
 Vasantharaju, N., Vemareddy, P., Ravindra, B., & Doddamani, V. H. 2019, *ApJ*, **874**, 182
 Vemareddy, P., Ambastha, A., & Maurya, R. A. 2012, *ApJ*, **761**, 60
 Vourlidas, A., Buzasi, D., & Howard, R. A. 2002, in *Solar Variability: From Core to Outer Frontiers* (The 10th European Solar Physics Meeting), ed. A. Wilson, Vol. 1 (Noordwijk: ESA Publications Division)
 Wang, H. 1992, *SoPh*, **140**, 85
 Wang, H., & Liu, C. 2010, *ApJL*, **716**, L195
 Wang, H., Spirock, T. J., Qiu, J., Ji, H., et al. 2002, *ApJ*, **576**, 497
 Wang, J., Simões, P. J. A., & Fletcher, L. 2018, *ApJ*, **859**, 25
 Wang, S., Liu, C., Liu, R., et al. 2012a, *ApJL*, **745**, L17
 Wang, S., Liu, C., & Wang, H. 2012b, *ApJL*, **757**, L5
 Wheatland, M. S., & Metcalf, T. R. 2006, *ApJ*, **636**, 1151
 Zharkova, V., & Zharkov, S. 2015, *SoPh*, **290**, 3163
 Zharkova, V. V., Zharkov, S. I., Ipson, S. S., & Benkhalil, A. K. 2005, *JGRA*, **110**, A08104